ACS APPLIED MATERIALS & INTERFACES

www.acsami.org

Research Article

Determining Surface Terminations and Chirality of Noncentrosymmetric FeGe Thin Films via Scanning Tunneling Microscopy

Joseph P. Corbett,* Tiancong Zhu, Adam S. Ahmed, Steven J. Tjung, Jacob J. Repicky, Takahiro Takeuchi, Jonathan Guerrero-Sanchez, Noboru Takeuchi, Roland K. Kawakami, and Jay A. Gupta

Cite This: *ACS Appl. Mater. Interfaces* 2020, 12, 9896–9901

Read Online

ACCESS | Metrics & More | Article Recommendations | Supporting Information

ABSTRACT: Scanning tunneling microscopy was used to study the surfaces of 20−100 nm thick FeGe films grown by molecular beam epitaxy. An average surface lattice constant of ∼6.8 Å, in agreement with the bulk value, was observed via scanning tunneling microscopy, low energy electron diffraction, and reflection high energy electron diffraction. Each of the four possible chemical terminations in the FeGe films were identified by comparing atomic-resolution images, showing distinct contrast with simulations from density functional theory calculations. A detailed study of the atomic layering order and registry across step edges allows us to uniquely determine the grain orientation and chirality in these noncentrosymmetric films.

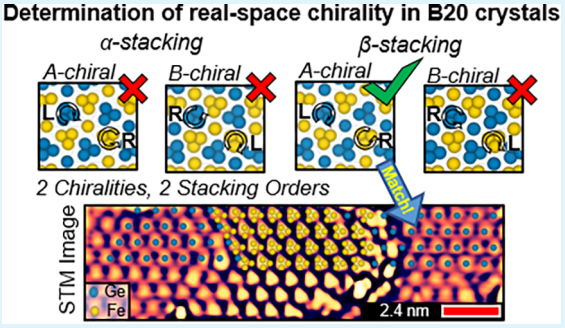

KEYWORDS: *chirality, FeGe, noncentrosymmetric, scanning tunneling microscopy, density functional theory, Tersoff−Hamann, B20, skyrmion*

1. INTRODUCTION

FeGe can crystallize into three polymorphs: a hexagonal phase, a monoclinic phase, and the cubic B20 phase[1] of interest here. The B20 family of materials (e.g., FeGe, MnSi, PdGa, AlPd, MnGe) have the interesting property of breaking inversion symmetry along the {111} planes, which has been shown to lead to magnetic skyrmions,[2−8] topologically protected spin textures.[9] Skyrmion sizes have been reported down to nanometer scales,[10−12] which is attractive for high density storage.[9,10,13−17] Though B20 FeGe hosts skyrmions in the bulk, there is interest in adding interfacial tuning to further decrease the skyrmion size while increasing the temperature stability.[5,17] Modifying the bulk Dzyaloshinskii−Moriya interaction via interfacial Rashba spin−orbit coupling[18,19] will depend in a sensitive manner on interface quality and chemical termination, which motivates investigations on epitaxial thin films with atomic-resolution imaging techniques.

Previous STM studies on B20 MnSi have revealed the characteristic layered structure and the coexistence of multiple surface terminations corresponding to sparse and dense atomic layers in the B20 unit cell.[20−23] These terminations were evident as terraces with distinct levels of corrugation in atomic-resolution images, separated by fractions of the characteristic B20 quadruple layer (QL) step height.[20−23] Density functional theory (DFT) has played an important role in understanding these materials, through calculations of surface free energies, confirming the possibility of multiple terminations as well as simulated STM images that can be directly compared with experiment.[20−23]

Here, we report a joint STM/DFT study in which we determine not only the surface terminations but also the real-space chirality of B20 crystals for the first time. Epitaxial B20 FeGe thin films were grown by molecular beam epitaxy (MBE). All four of the possible surface terminations were observed in atomic-resolution images as a triangular lattice of bright protrusions, but with distinct shape and atomic corrugation depending on the chemical identity. Through a detailed comparison of experimental STM images and spectroscopy with DFT simulations, we could assign the surface terminations to Fe-dense (Fe-d), Fe-sparse (Fe-s), Ge-dense (Ge-d), and Ge-sparse (Ge-s) layers and determine their stacking sequence in real space. Consideration of the registry between these layers then allowed us to determine the chirality of the surface region, which is difficult with ensemble techniques that typically require bulk single crystal samples. As the structural chirality sets the chirality of magnetic

Received: October 31, 2019
Accepted: January 27, 2020
Published: January 27, 2020

https://dx.doi.org/10.1021/acsami.9b19724
ACS Appl. Mater. Interfaces 2020, 12, 9896−9901

skyrmions in this family of materials,[24] this capability is important in harnessing these novel magnetic textures for future high density storage applications.

2. METHODS

Epitaxial FeGe thin films were grown on Si(111) substrates using a custom-built MBE system with a base pressure of ~1.0×10^{-10} Torr. The growth was monitored in real time with a 10 keV reflection high energy electron diffraction (RHEED) system from STAIB Instruments, whereas the fluxes were calibrated using a quartz crystal thickness monitor. The Si(111) substrates were prepared by ultrasonic precleaning with acetone and then isopropyl alcohol for 5 min each. The Si(111) substrate was subsequently dipped in a buffered HF solution for 2 min to chemically remove the oxide layer and H-terminate the Si(111) surface. The substrates were immediately transferred into the MBE chamber via a load lock to prevent reoxidation. The Si(111) substrates were then annealed at 800 °C for 20 min until RHEED showed a streaky 7 × 7 reconstruction pattern. The substrate was then cooled to the growth temperature of 300 °C, and Fe and Ge were co-deposited using thermal effusion cells with fluxes matched 1:1 in order to achieve a stoichiometric film. Films were grown with 20−100 nm thickness; all data reported here were on the 20 nm films but were consistent across samples. Further details and additional characterizations of the growth were reported previously.[18]

Shortly after growth, the FeGe samples were transferred in situ into a Ferrovac ultrahigh vacuum (UHV) suitcase with a base pressure of ~1.0×10^{-9} Torr and brought to another lab housing a Createc LT-STM system with its own UHV load lock and analysis chambers. LEED patterns were collected at normal incidence with a 140 eV beam energy to confirm crystallinity of the films. FeGe samples were directly transferred into the cold STM without any additional surface preparation to minimize contamination and preserve the as-grown film quality. STM measurements were performed at 5 K using cut PtIr tips. Tunneling spectra were obtained by disabling the STM feedback loop, adding a 20 mV modulation voltage to the DC sample bias, and using a lock-in amplifier to measure the corresponding modulation in tunneling current as the DC bias was swept. Image processing and analysis were performed using Gwyddion and WxSM for RHEED, LEED, and STM data.[25,26] Experimental data were compared against structural models built using the open-source VESTA software package.[27] Model structures used the bulk lattice constant of 664 pm for B20 FeGe and are available in the Supporting Information.

Spin-polarized density functional theory calculations, as implemented in the Quantum ESPRESSO package,[28] have been carried out to describe the atomic arrangements of the four possible FeGe surface terminations in each of the two stacking orders. The electronic states and the charge density were expanded in plane waves with energy cutoffs of 35 and 280 Ry, respectively. The exchange and correlation energies are calculated using the generalized gradient approximation as parametrized by Perdew−Burke−Ernzerhof.[29] The strong nuclear potential and the core electrons were replaced with ultrasoft pseudopotentials. In order to evaluate the electronic structure in the Brillouin zone, a 9 × 9 × 1 mesh of equally spaced k-points was used.[30] The atomic coordinates and electronic states were optimized until reaching the following convergence criteria: forces on each atom had to be smaller than 10 meV/Bohr and the energy differences lower than 1 meV.

To simulate the surface terminations, we started with 24 layer slabs with Fe-sparse and Ge-sparse surface terminations for the two stacking sequences and then recalculated with 23, 22, and 21 layers to simulate the other terminations in each sequence. In all cases, an empty space of 15 Å was included to eliminate undesirable interactions between the slab and its image generated due to the introduction of periodic conditions. Because the system has a ferromagnetic behavior, we have simulated ferromagnetic alignments in all configurations. To simulate the scanning tunneling microscopy images, we have used the Tersoff−Hamann approximation[31] as implemented in the Quantum ESPRESSO package (cf. Figure S3 for more information).

3. RESULTS AND DISCUSSION

Figure 1 illustrates the possible combinations of stacking order and chirality for grains in our B20 FeGe thin films. The QL

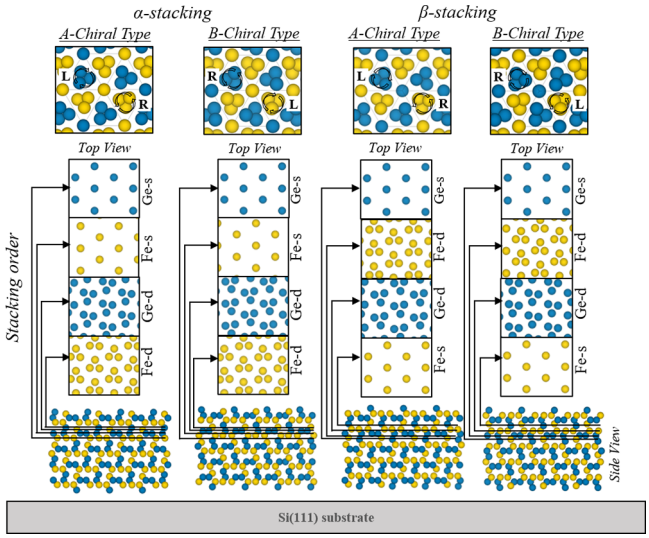

Figure 1. Model crystal structures for B20 FeGe. The two chiralities can be viewed from the spiraling of the Ge and Fe atoms from the {111} view (curved arrows in the top row of schematics). For each chirality, there are two distinct stacking orders, indicated with lines in one QL of the structure. For each of the four distinct combinations of chirality and stacking order, there are four possible surface terminations corresponding to sparse/dense packing of Fe/Ge. Each of these surface terminations produces a hexagonal lattice in the top view with the same lattice constant but distinct atomic arrangements. The combination of chirality, stacking order, and chemical termination leads to 16 possible unique surfaces.

structure comprises alternating Fe and Ge layers with sparse or dense packing. Sparse layers correspond to monomer Fe and Ge in a hexagonal lattice, whereas dense layers correspond to trimers of Fe and Ge arranged in the same lattice. Three QLs are needed before the atoms return to the same relative positions, resulting in a 12-layer unit cell. The $P2_13$ space group of the FeGe not only breaks inversion symmetry of the {111} planes but also leads to two possible stacking orders comprising a repeating sequence of [Ge-s, Fe-s, Ge-d, Fe-d] ("α-stacking") or [Ge-s, Fe-d, Ge-d, Fe-s] ("β-stacking") layers in order from surface to substrate. For each stacking order, the two chiralities can be visualized from the in-plane orientation of the trimers in the dense layers (see Figure 1).

In STM images of the surface, we observed regions with small terraces on top of ~10 nm scale grains as well as large grains over 100 nm × 100 nm in area with atomic scale steps. Up to four surface terminations can be observed in atomic-resolution images (e.g., Figure 2). These surfaces can be distinguished by the apparent atomic corrugation (ranging from ~5 to 40 pm) and the shape of the protrusions in the image (spherical or triangular).[23] Bright features in all of these regions define a hexagonal lattice with a lattice constant of ~6.9 Å, consistent with that expected for FeGe and confirmed with our LEED and RHEED measurements (cf. Figure S1).

To better understand these surface terminations, we focus on the flatter areas in large grains, where we can observe clearly

https://dx.doi.org/10.1021/acsami.9b19724
ACS Appl. Mater. Interfaces 2020, 12, 9896−9901

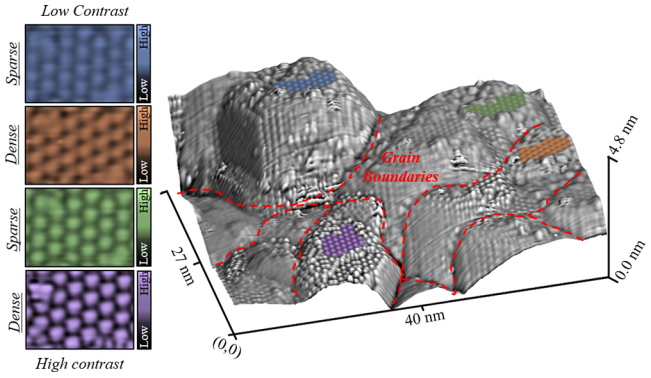

Figure 2. STM image resolving the four distinct terminations in FeGe. Right: 3D rendering of an STM image showing small faceted grains with distinct surface terminations. Grain boundaries are highlighted with dotted lines, and surface terminations at the tops of grains are highlighted in the higher-magnification images on the left. The four terminations exhibit increasing contrast (blue, orange, green, purple STM images) with spherical and triangular protrusions for sparse and dense-packed surfaces, respectively. Image taken at +1 V, 50 pA.

defined terraces separated by atomic step edges. Most of the step edges we observe on the surface correspond to multiples of 270 pm in apparent height, consistent with 1 QL for the FeGe B20 structure. However, there are some step edges with a fraction of the QL height. As shown in Figure 3a and the

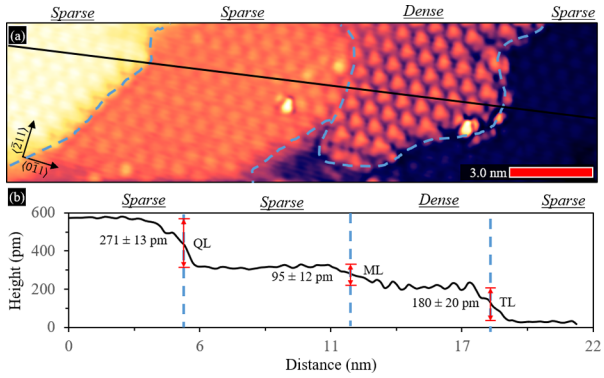

Figure 3. Identification of distinct terminations in neighboring terraces. (a) STM image showing neighboring terraces separated by QL and fractional QL steps. The contrast has been enhanced with Laplacian filtering. The terraces with spherically symmetric protrusions (sparse layer) are separated by QL steps, whereas the terrace with larger, more triangular contrast associated with a dense-packed surface is separated by ML and TL steps. (b) Line profile corresponding to the black line in (a). Topographic height differences corresponding to QL, ML, and TL steps are shown (+1 V, 50 pA).

corresponding line profile (Figure 3b), there is a 270 pm QL step down starting from the leftmost terrace, followed by smaller 95 and 170 pm steps. These are within uncertainty of the expected height differences for mono- (ML) and triple-layer (TL) steps between different chemical terminations in the layered FeGe B20 structure (cf., Figure 1). We note that, in general, there are topographic and electronic contributions to the apparent height in STM measurements. A true topographic height difference is only measured between two terraces if they have the same chemical termination. As a partial QL step moves between different terminations, the apparent step height is expected to be a mixture of electronic and topographic contributions. For the imaging conditions in Figure 3, the electronic contribution to the apparent height appears to be small given that we observe ML and TL steps with close to the crystallographic spacing.

To associate these terminations with the Fe and Ge layers in B20 FeGe, we performed a detailed comparison of experimental and DFT-simulated STM images. Figure 4a,b

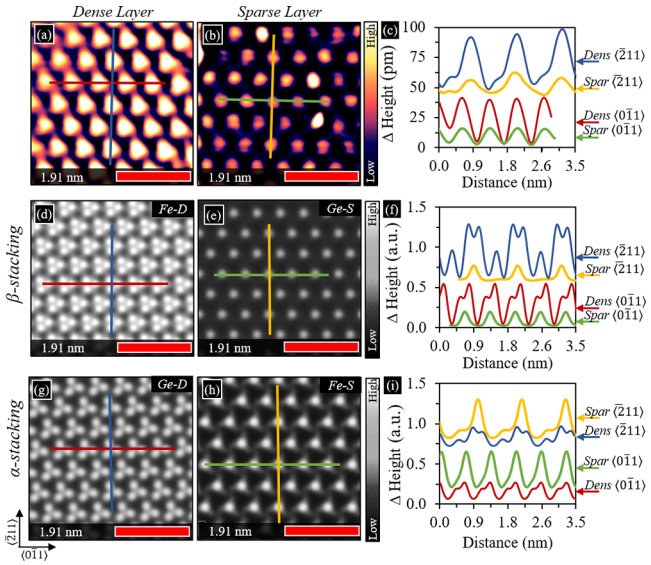

Figure 4. Comparison of STM and DFT-simulated images to assign chemical termination and stacking order. (a,b) High-resolution STM images of dense and sparse surfaces from Figure 3, showing the triangular-shaped and spherically symmetric protrusions, respectively. (c) Corresponding line profiles as color-coded in (a,b) along the [2̄11] and [01̄1] directions as shown. In both cases, the atomic corrugation in the dense-packed surface is higher (~40 pm) than that in the sparse-packed surface (~10 pm). (d–i) DFT-simulated STM images with the same layout as (a–c), corresponding to the two possible assignments of termination/stacking order. The simulated line profiles are offset for clarity, as indicated by the arrows in (f,i). For β-stacking, the highest corrugations are found for the Fe-d surface (red, blue lines in (f)) compared to the Ge-s surface, in agreement with the experimental trend in (c). In contrast, for α-stacking, the highest corrugation is observed on the Fe-s surface (yellow line in (i)), in disagreement with experiment (experiment: +1 V, 50 pA (a,b), theory: +1 V, 2.5 Å).

shows higher-magnification images of the two terraces separated by the ML step in Figure 3. We see distinct differences in the shape and atomic corrugation of the protrusions in these two images. We find that the protrusions in the higher contrast terrace are consistently triangular-shaped with different bias voltages and tip terminations, whereas the protrusions in the lower contrast terrace are more spherically symmetric. These qualitative differences are reproduced in DFT-simulated STM images of the sparse and dense surfaces. Shown in the Supporting Information (Figure S3) are simulated images for the eight possible combinations of surface termination and stacking order. As mentioned above, Fe- and Ge-dense surfaces represent a hexagonal lattice of trimers, and this results in triangular-shaped contrast in the simulated STM images, which do not significantly depend on stacking order. Sparse surfaces represent a hexagonal lattice of monomers, and this produces predominantly spherically symmetric contrast, with a small contribution from the

https://dx.doi.org/10.1021/acsami.9b19724
ACS Appl. Mater. Interfaces 2020, 12, 9896–9901

underlayer that depends on stacking order. This suggests that the terrace with the spherically symmetric protrusions is either a Ge-sparse or Fe-sparse surface and the ML step down must be to an Fe-dense or Ge-dense surface, respectively. Thus, the sparse/dense distinction and the ML step height difference allows us to narrow the list of grain possibilities to two, one for each stacking order, as shown in the simulated STM images in Figure 4d,e and g,h and illustrated schematically in Figure 1.

Comparison of the observed and predicted atomic corrugations then allows us to complete the assignment. Figure 4c shows line profiles from the experimental images, taken along the $\{\bar{2}11\}$ and $\{0\bar{1}1\}$ directions for both surfaces. For the lower contrast sparse surface, the atomic corrugation is ~10 pm (yellow and green profiles), whereas for the higher contrast dense surface, a corrugation of ~40 pm is observed (red and blue profiles). We compared these observations with the apparent height corrugation in the simulated STM images (Figure 4f,i) for the two possibilities. We find the general trend that, regardless of packing or stacking order, Fe-terminated surfaces have an atomic corrugation significantly higher than that of Ge-terminated surfaces. Thus, we assign the higher corrugation dense surface in Figure 4a to the Fe-dense termination and the lower corrugation sparse surface to the Ge-sparse termination. The ML step down from Ge-s to Fe-d thus reflects the β-stacking sequence [Ge-s, Fe-d, Ge-d, Fe-s] in order from surface toward substrate.

Shown in the Supporting Information (Figure S4) is a comparison of experimental tunneling spectra and calculated local density of states (LDOS), which are in qualitative agreement with this assignment. The calculations show a significantly higher LDOS associated with the Fe-d layer as compared to that of the Ge-s layer for this stacking order, which is consistent with the experimental tunneling spectra. For α-stacking, there is little difference in LDOS between the Fe-s and Ge-d surfaces in the energy window of interest, except for a pronounced peak in unoccupied states for the Fe-s surface that is not observed in the experiment. This further supports our assignment of the high contrast terrace with triangular protrusions to the Fe-d termination and the low contrast surface with spherical protrusions to the Ge-s termination.

We now closely look at the atomic registry between Ge-s and Fe-d lattices to determine the grain chirality. Shown in Figure 5 is a higher magnification STM image of the region in Figure 4, with atomic overlays corresponding to *A*- and *B*-type chiralities for the β-stacking order. These overlays represent cuts of the bulk crystal at one of the surface terminations and then selective removal of layers to model the ML and TL steps in this region. For each chirality, we aligned the trimers in the Fe-dense layer with the observed contrast and extended the resultant lattices for the Ge-sparse layers onto the adjacent terraces. In this way, we see that the registry of the Ge-s layers with the bright protrusions in the STM image is in close agreement for *A*-type chirality (Figure 5a) but is off on one terrace for *B*-type chirality (Figure 5b). Thus, we are able to uniquely determine the stacking orientation and chirality of this grain (β-stacking, *A*-type chirality) through a detailed comparison of STM and DFT data and analysis of the atomic registry across ML steps.

In the Supporting Information (Figure S6), we present a similar analysis of another region of the sample which showed three surface terminations (Fe-s, Ge-s, and Ge-d), all separated by fractional QL steps. By again considering the symmetry of the lattice points (triangular vs spherical), the apparent

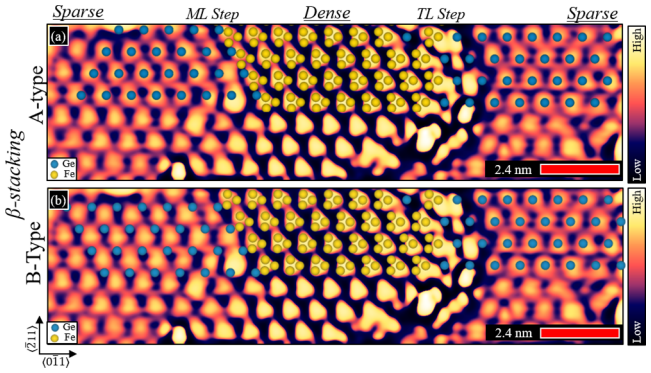

Figure 5. Determination of chirality from atomic lattice registries. (a,b) Atomic-resolution STM image of the neighboring Ge-s/Fe-d/Ge-s terraces in Figure 3, with lattice overlays corresponding to *A*-type (a) and *B*-type (b) chiralities. Fe-d trimers are aligned with the triangular protrusions in the experimental image in both cases. The lattice of neighboring Ge-s layers is extended to the left up a ML step and to the right down a TL step, according to the crystal model in Figure 1. Because the two chiralities have distinct relative atomic positions, the Ge-s lattices on both sides only agree with experiment for *A*-type chirality, whereas there is a misalignment for *B*-type chirality on the left Ge-s terrace. STM images were Laplace-filtered to emphasize local contrast (+1 V, 50 pA).

corrugation, and the layering order, we were able to assign the chemical terminations and determine the α-stacking sequence [Ge-s, Fe-s, Ge-d, Fe-d] in this case. *B*-type chirality was determined for this region by comparing the registry across ML and TL steps between Fe-s and Ge-d terraces.

In larger surveys of the surface, we found that the Fe-s and Ge-s terminations predominate, with only small terraces of dense terminations. This suggests that the sparse surfaces have lower free energies under our growth conditions. Additional DFT calculations show that all four terminations are very close in surface formation energy (Figure S2). This suggests that coexistence of terminations on the surface is likely and may sensitively depend on local growth conditions. It would be interesting to repeat such a survey for grain chiralities using these methods to determine if the choice of substrate or growth methods can preferentially select for one chirality over the other.[24,32]

4. CONCLUSIONS

In summary, a detailed comparison of experimental STM data and DFT calculations allowed us to identify the four distinct surface terminations in the B20 FeGe structure. The stacking order and grain chirality were then found considering atomic-resolution images of terraces separated by fractional QL steps. These methods can be used to inform future spin-resolved microscopy measurements, not only in the B20 family but also in other layered, chiral or noncollinear ferro- and antiferromagnetic systems. Racetrack designs for skyrmions in such systems are of increasing interest for future high density storage applications.[33−35]

■ ASSOCIATED CONTENT

Supporting Information

The Supporting Information is available free of charge at https://pubs.acs.org/doi/10.1021/acsami.9b19724.

https://dx.doi.org/10.1021/acsami.9b19724
ACS Appl. Mater. Interfaces 2020, 12, 9896−9901

Additional STM and DFT data that more fully explain the methodologies for surface termination and chirality assignments and a second region for analysis (PDF)

AUTHOR INFORMATION

Corresponding Author

Joseph P. Corbett − *Department of Physics, The Ohio State University, Columbus, Ohio 43210, United States;* orcid.org/0000-0002-9819-8574; Email: corbett.123@osu.edu

Authors

Tiancong Zhu − *Department of Physics, The Ohio State University, Columbus, Ohio 43210, United States*

Adam S. Ahmed − *Department of Physics, The Ohio State University, Columbus, Ohio 43210, United States*

Steven J. Tjung − *Department of Physics, The Ohio State University, Columbus, Ohio 43210, United States;* orcid.org/0000-0002-1386-2828

Jacob J. Repicky − *Department of Physics, The Ohio State University, Columbus, Ohio 43210, United States*

Takahiro Takeuchi − *Integrated Graduate School of Medicine, Engineering, and Agricultural Science, University of Yamanashi, Kofu 400-8510, Japan*

Jonathan Guerrero-Sanchez − *Centro de Nanociencias y Nanotecnologia, Universidad Nacional Autónoma de México, Ensenada, Baja California 22800, Mexico*

Noboru Takeuchi − *Centro de Nanociencias y Nanotecnologia, Universidad Nacional Autónoma de México, Ensenada, Baja California 22800, Mexico*

Roland K. Kawakami − *Department of Physics, The Ohio State University, Columbus, Ohio 43210, United States;* orcid.org/0000-0003-0245-9192

Jay A. Gupta − *Department of Physics, The Ohio State University, Columbus, Ohio 43210, United States*

Complete contact information is available at: https://pubs.acs.org/10.1021/acsami.9b19724

Author Contributions

J.P.C. performed the analysis and contributed to writing the manuscript. A.A. grew the samples. T.Z., S.J.T., J.J.R., and T.T. performed the measurements. J.G.-S. and N.T. performed the DFT calculations. R.K.K. and J.A.G. contributed to the manuscript writing.

Notes

The authors declare no competing financial interest.

ACKNOWLEDGMENTS

We acknowledge support from DARPA (Grant No. D18AP00008) and DOE (DE-SC0016379). The authors thank R.K. Smith for useful discussions. J.G.S. and N.T. thank DGAPA-UNAM project IN101019 and CONACyT (Grant No. A1-S-9070) for partial financial support. Calculations were performed in the DGCTIC-UNAM Supercomputing Center, project LANCAD-UNAM-DGTIC-368. See arXiv for preprint version of this manuscript.[36]

REFERENCES

(1) Zeng, C.; Kent, P. R. C.; Varela, M.; Eisenbach, M.; Stocks, G. M.; Torija, M.; Shen, J.; Weitering, H. H. Epitaxial Stabilization of Ferromagnetism in the Nanophase of FeGe. *Phys. Rev. Lett.* **2006**, *96*, 127201−127205.

(2) Zhao, X.; Jin, C.; Wang, C.; Du, H.; Zang, J.; Tian, M.; Che, R.; Zhang, Y. Direct Imaging of Magnetic Field-Driven Transitions of Skyrmion Cluster States in FeGe Nanodisks. *Proc. Natl. Acad. Sci. U. S. A.* **2016**, *113*, 4918−4923.

(3) Turgut, E.; Paik, H.; Nguyen, K.; Muller, D. A.; Schlom, D. G.; Fuchs, G. D. Engineering Dzyaloshinskii-Moriya Interaction in B20 Thin-Film Chiral Magnets. *Phys. Rev. Mater.* **2018**, *2*, 074404−8.

(4) Yu, X. Z.; Kanazawa, N.; Onose, Y.; Kimoto, K.; Zhang, W. Z.; Ishiwata, S.; Matsui, Y.; Tokura, Y. Near Room-Temperature Formation of a Skyrmion Crystal in Thin-Films of the Helimagnet FeGe. *Nat. Mater.* **2011**, *10*, 106−109.

(5) Huang, S. X.; Chien, C. L. Extended Skyrmion Phase in Epitaxial FeGe (111) Thin Films. *Phys. Rev. Lett.* **2012**, *108*, 267201−5.

(6) Uchida, M.; Nagaosa, N.; He, J. P.; Kaneko, Y.; Iguchi, S.; Matsui, Y.; Tokura, Y. Topological Spin Textures in the Helimagnet FeGe. *Phys. Rev. B: Condens. Matter Mater. Phys.* **2008**, *77*, 184402−5.

(7) Muhlbauer, S.; Binz, B.; Jonietz, F.; Pfleiderer, C.; Rosch, A.; Neubauer, A.; Georgii, R.; Boni, P. Skyrmion Lattice in a Chiral Magnet. *Science* **2009**, *323*, 915−919.

(8) Heinze, S.; von Bergmann, K.; Menzel, M.; Brede, J.; Kubetzka, A.; Wiesendanger, R.; Bihlmayer, G.; Blügel, S. Spontaneous Atomic-Scale Magnetic Skyrmion Lattice in Two Dimensions. *Nat. Phys.* **2011**, *7*, 713−718.

(9) Wiesendanger, R. Nanoscale Magnetic Skyrmions in Metallic Films and Multilayers: A New Twist for Spintronics. *Nat. Rev. Mater.* **2016**, *1*, 16044.

(10) Jiang, W.; Upadhyaya, P.; Zhang, W.; Yu, G.; Jungfleisch, M. B.; Fradin, F. Y.; Pearson, J. E.; Tserkovnyak, Y.; Wang, K. L.; Heinonen, O.; te Velthuis, S. G. E.; Hoffmann, A. Blowing Magnetic Skyrmion Bubbles. *Science* **2015**, *349*, 283−286.

(11) Tanigaki, T.; Shibata, K.; Kanazawa, N.; Yu, X.; Onose, Y.; Park, H. S.; Shindo, D.; Tokura, Y. Real-Space Observation of Short-Period Cubic Lattice of Skyrmions in MnGe. *Nano Lett.* **2015**, *15*, 5438−5442.

(12) Grenz, J.; Köhler, A.; Schwarz, A.; Wiesendanger, R. Probing the Nano-Skyrmion Lattice on Fe/Ir(111) with Magnetic Exchange Force Microscopy. *Phys. Rev. Lett.* **2017**, *119*, 047205−4.

(13) Fert, A.; Cros, V.; Sampaio, J. Skyrmions on the Track. *Nat. Nanotechnol.* **2013**, *8*, 152−156.

(14) Fert, A.; Reyren, N.; Cros, V. Magnetic Skyrmions: Advances in Physics and Potential Applications. *Nat. Rev. Mater.* **2017**, *2*, 17031.

(15) Koshibae, W.; Kaneko, Y.; Iwasaki, J.; Kawasaki, M.; Tokura, Y.; Nagaosa, N. Memory Functions of Magnetic Skyrmions. *Jpn. J. Appl. Phys.* **2015**, *54*, 053001−053009.

(16) Tomasello, R.; Martinez, E.; Zivieri, R.; Torres, L.; Carpentieri, M.; Finocchio, G. A Strategy for the Design of Skyrmion Racetrack Memories. *Sci. Rep.* **2015**, *4*, 6784.

(17) Yu, G.; Upadhyaya, P.; Shao, Q.; Wu, H.; Yin, G.; Li, X.; He, C.; Jiang, W.; Han, X.; Amiri, P. K.; Wang, K. L. Room-Temperature Skyrmion Shift Device for Memory Application. *Nano Lett.* **2017**, *17*, 261−268.

(18) Ahmed, A. S.; Esser, B. D.; Rowland, J.; McComb, D. W.; Kawakami, R. K. Molecular Beam Epitaxy Growth of [CrGe/MnGe/FeGe] Superlattices: Toward Artificial B20 Skyrmion Materials with Tunable Interactions. *J. Cryst. Growth* **2017**, *467*, 38−46.

(19) Rowland, J.; Banerjee, S.; Randeria, M. Skyrmions in Chiral Magnets with Rashba and Dresselhaus Spin-Orbit Coupling. *Phys. Rev. B: Condens. Matter Mater. Phys.* **2016**, *93*, 020404−020409.

(20) Geisler, B.; Kratzer, P.; Suzuki, T.; Lutz, T.; Costantini, G.; Kern, K. Growth Mode and Atomic Structure of MnSi Thin Films on Si(111). *Phys. Rev. B: Condens. Matter Mater. Phys.* **2012**, *86*, 115428−7.

(21) Azatyan, S. G.; Utas, O. A.; Denisov, N. V.; Zotov, A. V.; Saranin, A. A. Variable Termination of MnSi/Si(111) $\sqrt{3} \times \sqrt{3}$ Films and its Effect on Surface Properties. *Surf. Sci.* **2011**, *605*, 289−295.

(22) Suzuki, T.; Lutz, T.; Geisler, B.; Kratzer, P.; Kern, K.; Costantini, G. Surface Morphology of MnSi Thin Films Grown on Si(111). *Surf. Sci.* **2013**, *617*, 106−112.

(23) Krajčí, M.; Hafner, J. Surfaces of Intermetallic Compounds: An *Ab Initio* DFT Study for B20-Type AlPd. *Phys. Rev. B: Condens. Matter Mater. Phys.* **2013**, *87*, 035436.
(24) Grigoriev, S. V.; Potapova, N. M.; Siegfried, S.-A.; Dyadkin, V. A.; Moskvin, E. V.; Dmitriev, V.; Menzel, D.; Dewhurst, C. D.; Chernyshov, D.; Sadykov, R. A.; Fomicheva, L. N.; Tsvyashchenko, A. V. Chiral Properties of Structure and Magnetism in Mn1−xFexGe Compounds: When the Left and the Right are Fighting, Who Wins? *Phys. Rev. Lett.* **2013**, *110*, 207201−5.
(25) Horcas, I.; Fernández, R.; Gómez-Rodríguez, J. M.; Colchero, J.; Gómez-Herrero, J.; Baro, A. M. WSXM: A Software for Scanning Probe Microscopy and a Tool for Nanotechnology. *Rev. Sci. Instrum.* **2007**, *78*, 013705−8.
(26) Nečas, D.; Klapetek, P. Gwyddion: An Open-Source Software for SPM Data Analysis. *Cent. Eur. J. Phys.* **2012**, *10*, 181−188.
(27) Momma, K.; Izumi, F. VESTA 3 for Three-Dimensional Visualization of Crystal, Volumetric and Morphology Data. *J. Appl. Crystallogr.* **2011**, *44*, 1272−1276.
(28) Giannozzi, P.; Baroni, S.; Bonini, N.; Calandra, M.; Car, R.; Cavazzoni, C.; Ceresoli, D.; Chiarotti, G. L.; Cococcioni, M.; Dabo, I.; Dal Corso, A.; de Gironcoli, S.; Fabris, S.; Fratesi, G.; Gebauer, R.; Gerstmann, U.; Gougoussis, C.; Kokalj, A.; Lazzeri, M.; Martin-Samos, L.; Marzari, N.; Mauri, F.; Mazzarello, R.; Paolini, S.; Pasquarello, A.; Paulatto, L.; Sbraccia, C.; Scandolo, S.; Sclauzero, G.; Seitsonen, A. P.; Smogunov, A.; Umari, P.; Wentzcovitch, R. M. QUANTUM ESPRESSO: A Modular and Open-Source Software Project for Quantum Simulations of Materials. *J. Phys.: Condens. Matter* **2009**, *21*, 395502−395521.
(29) Perdew, J. P.; Burke, K.; Ernzerhof, M. Generalized Gradient Approximation Made Simple. *Phys. Rev. Lett.* **1996**, *77*, 3865−3868.
(30) Monkhorst, H. J.; Pack, J. D. Special Points for Brillouin-Zone Integrations. *Phys. Rev. B* **1976**, *13*, 5188−5192.
(31) Tersoff, J.; Hamann, D. R. Theory of the Scanning Tunneling Microscope. *Phys. Rev. B: Condens. Matter Mater. Phys.* **1985**, *31*, 805−813.
(32) Grigoriev, S. V.; Chernyshov, D.; Dyadkin, V. A.; Dmitriev, V.; Maleyev, S. V.; Moskvin, E. V.; Menzel, D.; Schoenes, J.; Eckerlebe, H. Crystal Handedness and Spin Helix Chirality in Fe1-xCoxSi. *Phys. Rev. Lett.* **2009**, *102*, 037204−4.
(33) Jungwirth, T.; Marti, X.; Wadley, P.; Wunderlich, J. Antiferromagnetic Spintronics. *Nat. Nanotechnol.* **2016**, *11*, 231−241.
(34) Parkin, S.; Yang, S.-H. Memory on the Racetrack. *Nat. Nanotechnol.* **2015**, *10*, 195−198.
(35) Liang, X.; Zhao, G.; Shen, L.; Xia, J.; Zhao, L.; Zhang, X.; Zhou, Y. Dynamics of an Antiferromagnetic Skyrmion in a Racetrack with a Defect. *Phys. Rev. B: Condens. Matter Mater. Phys.* **2019**, *100*, 144439−8.
(36) Corbett, J. P.; Zhu, T.; Ahmed, A. S.; Tjung, S. J.; Repicky, J. J.; Takeuchi, T.; Kawakami, R. K.; Gupta, J. A. Surface Structures of Epitaxial B20 FeGe(−1−1−1) Thin Films via Scanning Tunneling Microscopy. arXiv:1807.00741v1 2018.

https://dx.doi.org/10.1021/acsami.9b19724
ACS Appl. Mater. Interfaces 2020, 12, 9896−9901